Detection efficiency in total internal reflection fluorescence microscopy

Marcel Leutenegger, Theo Lasser

Laboratoire d'Optique Biomédicale, École Polytechnique Fédérale de Lausanne, 1015 Lausanne, Switzerland

http://lob.epfl.ch/

Abstract: We present a rapid and flexible framework for the accurate calculation of the detection efficiency of fluorescence emission in isotropic media as well as in the vicinity of dielectric or metallic interfaces. The framework accounts for the dipole characteristics of the emitted fluorescence and yields the absolute detection efficiency by taking into account the total power radiated by the fluorophore. This analysis proved to be useful for quantitative measurements, i.e. the fluorescence detection at a glass–water interface for total internal reflection fluorescence microscopy in an epi- and a trans-illumination configuration.

OCIS codes: (180.2520) Microscopy, fluorescence microscopy; (110.2990) Imaging systems, image formation theory; (180.6900) Microscopy, three-dimensional microscopy; (240.6490) Spectroscopy, surface.

References and links

1. D. Magde, W. W. Webb, E. Elson, "Thermodynamic fluctuations in a reacting system - measurement by fluorescence correlation spectroscopy," Phys. Rev. Lett. **29,** 705 (1972).
2. R. Rigler, E. S. Elson, *Fluorescence Correlation Spectroscopy: Theory and Applications*, Springer Ser. Chem. Phys. **65,** ISBN 3-540-67433-0 (2001).
3. P. Kask, K. Palo, D. Ullmann, K. Gall, "Fluorescence-intensity distribution analysis and its application in biomolecular detection technology," PNAS **96,** 13756–13761 (1999).
4. Y. Chen, J. D. Müller, P. T. C. So, E. Gratton, "The Photon Counting Histogram in Fluorescence Fluctuation Spectroscopy," Biophys. J. **77,** 553–567 (1999).
5. C. Eggeling, P. Kask, D. Winkler, S. Jäger, "Rapid Analysis of Förster Resonance Energy Transfer by Two-Color Global Fluorescence Correlation Spectroscopy: Trypsin Proteinase Reaction," Biophys. J. **89,** 605–618 (2005).
6. J. Enderlein, I. Gregor, D. Patra, T. Dertinger, U. B. Kaupp, "Performance of Fluorescence Correlation Spectroscopy for Measuring Diffusion and Concentration," ChemPhysChem **6,** 2324–2336 (2005).
7. P. Török, P. D. Higdon, T. Wilson, "Theory for confocal and conventional microscopes imaging small dielectric scatterers," J. Mod. Opt. **45,** 1681–1698 (1998).
8. P. D. Higdon, P. Török, T. Wilson, "Imaging properties of high aperture multiphoton fluorescence scanning optical microscopes," J. Microsc. **193,** 127–141 (1999).
9. P. Török, "Propagation of electromagnetic dipole waves through dielectric interfaces," Opt. Lett. **25,** 1463–1465 (2000).
10. J. Enderlein, M. Böhmer, "Influence of interfacedipole interactions on the efficiency of fluorescence light collection near surfaces," Opt. Lett. **28,** 941–943 (2003).
11. P. Debye, "Das Verhalten von Lichtwellen in der Nähe eines Brennpunktes oder einer Brennlinie," Ann. Phys. **30,** 755–776 (1909).
12. E. Wolf, "Electromagnetic diffraction in optical systems, I. An integral representation of the image field," Proc. R. Soc. London Ser. A **253,** 349–357 (1959).
13. B. Richards, E. Wolf, "Electromagnetic diffraction in optical systems, II. Structure of the image field in an aplanatic system," Proc. R. Soc. London Ser. A **253,** 358–379 (1959).
14. M. Leutenegger, R. Rao, R. A. Leitgeb, T. Lasser, "Fast focus field calculations," Opt. Express **14,** 11277–11291 (2006).

#94399 - $15.00 USD Received 28 Mar 2008; revised 9 May 2008; accepted 23 May 2008; published 27 May 2008

15. The subscript refers to the wavelength used for calculating the corresponding quantity.
16. B. Valeur, *Molecular fluorescence: principles and applications*, Wiley-VCH, ISBN 3-527-29919-X (2002).
17. J. Widengren, P. Schwille, "Characterization of Photoinduced Isomerization and Back-Isomerization of the Cyanine Dye Cy5 by Fluorescence Correlation Spectroscopy," J. Phys. Chem. A **104,** 6416–6428 (2000).
18. C. Eggeling, A. Volkmer, C. A. M. Seidel, "Molecular Photobleaching Kinetics of Rhodamine 6G by One- and Two-Photon Induced Confocal Fluorescence Microscopy," Chem. Phys. Chem. **6,** 791–804 (2005).
19. W. Lukosz, R. E. Kunz, "Light-emission by magnetic and electric dipoles close to a plane interface: 1. Total radiated power," J. Opt. Soc. Am. **67,** 1607–1615 (1977).
20. W. Lukosz, "Light-emission by magnetic and electric dipoles close to a plane dielectric interface: 3. Radiation-patterns of dipoles with arbitrary orientation," J. Opt. Soc. Am. **69,** 1495–1503 (1979).
21. T. P. Burghardt, N. L. Thompson, "Effect of planar dielectric interfaces on fluorescence emission and detection. Evanescent excitation with high-aperture collection," Biophys. J. **46,** 729–737 (1984).
22. E. H. Hellen, D. Axelrod, "Fluorescence emission at dielectric and metal-film interfaces," J. Opt. Soc. Am. B **4,** 337–350 (1987).
23. L. Novotny, "Allowed and forbidden light in near-field optics. II. Interacting dipolar particles," J. Opt. Soc. Am. A **14,** 105–113 (1997).
24. J. Mertz, "Radiative absorption, fluorescence, and scattering of a classical dipole near a lossless interface: a unified description," J. Opt. Soc. Am. B **17,** 1906–1913 (2000).
25. G. W. Ford, W. H. Weber, "Electromagnetic interactions of molecules with metal surfaces," Phys. Rep. **113,** 195–287 (1984).
26. J. Enderlein, T. Ruckstuhl, "The efficiency of surface-plasmon coupled emission for sensitive fluorescence detection," Opt. Express **13,** 8855–8865 (2005).
27. F. D. Stefani, K. Vasilev, N. Bocchio, N. Stoyanova, M. Kreiter, "Surface-plasmon-mediated single-molecule fluorescence through a thin metallic film," Phys. Rev. Lett. **94,** 023005 (2005).
28. E. H. Hellen, D. Axelrod, "Fluorescence emission at dielectric and metal-film interfaces," J. Opt. Soc. Am. B **4,** 337–350 (1987).
29. J. R. Lakowicz, J. Malicka, I. Gryczynski, Z. Gryczynski, C. D. Geddes, "Radiative decay engineering: the role of photonic mode density in biotechnology," J. Phys. D: Appl. Phys. **36,** R240–R249 (2003).
30. For single photon detectors SPCM-AQR-xx by PerkinElmer, $q_d \approx 55\%$ at $\lambda_{fl} = 525$nm, respectively $q_d \approx 45\%$ for the PDM 50CT by Micro Photon Devices.
31. Typical values: $\approx 85\%$ transmission through the dichroic mirror and $\approx 90\%$ transmission through the emission bandpass filter with a bandwidth covering $\approx 60\%$ of the fluorescence spectrum, that is $T_{fl} \approx 45\%$ in total.
32. R. J. Potton, "Reciprocity in optics," Rep. Prog. Phys. **67,** 717–754 (2004).
33. J.-L. Kaiser, E. Quertemont, R. Chevallier, "Light propagation in the pseudo-paraxial Fresnel approximation," Opt. Commun. **233,** 261–269 (2004).
34. A. E. Siegman, *Lasers*, Oxford Univ. Press, ISBN 0-19-855713-2 (1986).
35. D. Mas, J. Garcia, C. Ferreira, L. M. Bernardo, F. Marinho, "Fast algorithms for free-space diffraction patterns calculation," Opt. Commun. **164,** 233–245 (1999).
36. The Royal microscope standard limits the clear objective aperture to less than 16mm. The shortest commercial tube length is 164mm (Carl Zeiss), which yields an image NA < 8mm/164mm = 0.049.
37. According to previous notes $q_d T_{fl} \approx 23\%$ typically.
38. A. M. Lieto, R. C. Cush, N. L. Thompson, "Ligand-Receptor Kinetics Measured by Total Internal Reflection with Fluorescence Correlation Spectroscopy," Biophys. J. **85,** 3294–3302 (2003).
39. M. Leutenegger, H. Blom, J. Widengren, C. Eggeling, M. Gösch, R. A. Leitgeb, T. Lasser, "Dual-color total internal reflection fluorescence cross-correlation spectroscopy," J. Biomed. Opt. **11,** 040502 (2006).
40. K. Hassler, M. Leutenegger, P. Rigler, R. Rao, R. Rigler, M. Gösch, T. Lasser, "Total internal reflection fluorescence correlation spectroscopy (TIR-FCS) with low background and high count-rate per molecule," Opt. Express **13,** 7415–7423 (2005).

1. Introduction

Modern fluorescence microscopy provides outstanding spatio-temporal resolution, sensitivity and selectivity for investigating biological samples at the sub-micrometer scale. Due to these properties, it has become the method of choice in life science and biomedical research. Besides impressive improvements in image resolution and contrast, the need for quantitative measurements becomes more and more important. Fluorescence fluctuation spectroscopy (FFS) with correlation analysis (FCS) [1, 2], intensity distribution analysis (FIDA, PCH) [3, 4] or Förster resonant energy transfer (FRET) [5] addresses these demands. For these quantitative measurements, knowledge of the optical point spread function is required. This corresponds to the

#94399 - $15.00 USD Received 28 Mar 2008; revised 9 May 2008; accepted 23 May 2008; published 27 May 2008

brightness profile of the detected fluorescence, which demands the combined calculation of the excitation focus field, the response of fluorescent markers and finally the detection efficiency. This allows accurately modeling and predicting the measured fluorescence signal as recently shown in detail by Enderlein et al. [6]. The physical concepts of focusing electromagnetic waves and detecting dipole waves are well-known and described for instance by Török, Higdon and Enderlein [7, 8, 9, 10]. In analogy to the classical Debye formulation [11] and the seminal work by Wolf and Richards [12, 13], we recently reformulated the calculation of the electromagnetic field in the focus of high numerical aperture objectives based on a Fourier or chirp z transform [14] and achieved unprecedented calculation speed and flexibility. These calculations yet describe the excitation fields and thereby the excitation rates of fluorophores within these foci. In this work, we revisit the induced fluorescence emission based on the classical reciprocity principle in order to calculate accurately the detection efficiency within the same rapid and flexible framework. Our calculation accounts for the anisotropic distribution of the emitted fluorescence and yields the absolute detection efficiency through normalization with the total radiated power of the fluorophore [10].

Without any restriction, we assume that the biological sample is contained in water. The induced fluorescence response can be caused by auto-fluorescence or specific biomarkers. Based on a classical description, the fluorophore is described as a dipole absorbing photons at the excitation wavelength λ_{ex} and responding by the emission of fluorescence within a wavelength range λ_{fl}, where $\lambda_{fl} \gtrsim \lambda_{ex}$ due to the Stokes shift. Under these general assumptions, the total fluorescence process can be described by:

1. the excitation field $\vec{E}_{ex}(\vec{r},t)$,
2. the excitation cross-section $\overleftrightarrow{\sigma}_{ex}(\vec{r},\Omega)$ and the excitation rate $R_{ex}(\vec{r},\Omega,t)$ of the fluorophore,
3. the photophysical and photochemical response of the fluorophore,
4. the emission rate $R_{fl}(\vec{r},\Omega,t)$ of the fluorophore,
5. the emitted field $\vec{E}_{fl}(\vec{r},\Omega)$ from the fluorophore and
6. the detection efficiency $Q_{fl}(\vec{r},\Omega)$ of this radiation,
7. which altogether yield the fluorescence signal $I(t)$ from the sample.

All these quantities vary in general with the position $\vec{r} = (x,y,z)$ of the fluorophore and the orientation $\Omega = (\Theta,\varphi)$ of its absorption and emission dipoles upon absorption and emission, respectively, as well as with the wavelength of excitation and emission [15]. The calculation of the excitation field (1) is described in a former publication [14] and is used as a conceptual framework for the field calculations. The average excitation cross-section σ_{ex} (2) as provided by the manufacturer is typically in the order of a few Å^2. The general fluorophore response (3) is well described by B. Valeur [16] for instance. The specific photophysical response of Cy5 was investigated by Widengren and Schwille [17], whereas Eggeling et al. [18] recently reviewed the photochemical response of Rhodamine 6G. In this work, we focus on the calculation of the emission rate (4), the emitted field (5) and the detection efficiency (6). As a final demonstration, we calculate the fluorescence detection at a glass–water interface and compare the detection yields for total internal reflection fluorescence (TIRF) microscopy in an epi- and a trans-illumination configuration.

Throughout this paper, we omit the time dependency $\exp(-i\omega t)$. $\omega = 2\pi c_0/\lambda$ is the angular frequency, c_0 the speed of light and λ the wavelength in free space. Further we assume a relative

#94399 - $15.00 USD Received 28 Mar 2008; revised 9 May 2008; accepted 23 May 2008; published 27 May 2008

magnetic permeability $\mu_r = 1$ for all materials. Therefore, the refraction index n is given by the dielectric permittivity $\epsilon_r = n^2$. In order to avoid sign ambiguities in $k_z^2 = k^2 - k_{xy}^2$, we keep all wavevectors $\vec{k}$ pointing towards the positive z-axis with a proper sign choice for k_z.

2. Emission close to planar interfaces

This section describes the interaction of a fluorophore with planar layers and derives the emission rate $R_{fl}(\vec{r},\Omega)$, where $\vec{r}$ is the position of the fluorophore and $\Omega = (\Theta,\varphi)$ its orientation as shown in Fig. 1. The fluorophore is modeled as a point dipole with fixed dipole moment $\vec{\mu}$.

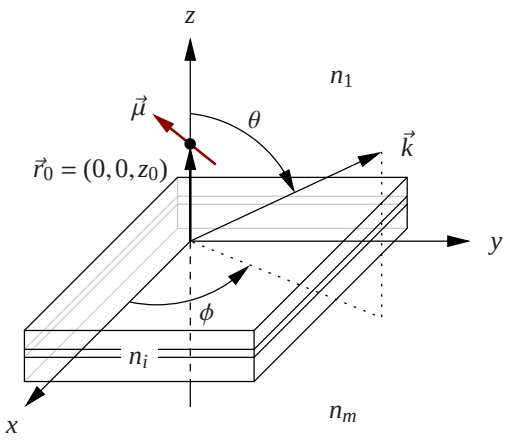

Fig. 1. Dipole $\vec{\mu}$ located at $\vec{r}_0$ above the first interface. n_1 is the refraction index of the upper half-space ($z > 0$) around the dipole. n_m is the refraction index of the lower half-space ($z < -d$) and n_i the refraction indices of the intermediate layers ($-d < z < 0$).

The dissipated power is given in a semi-classical picture by the dipole–light interaction. In a quantum-mechanical description, the dissipated power is analyzed with the transition probabilities and results in equivalent formulae, where the decay rate Γ of an electronic state defines the overall rate of all de-excitation channels from that state. In general, Γ contains a radiative decay Γ_{em} and a non-radiative decay Γ_{nr} and is simply the sum of both.

$$\Gamma(\vec{r},\Omega) = \Gamma_{em}(\vec{r},\Omega) + \Gamma_{nr} \tag{1}$$

Γ_{em} is associated with electromagnetic radiation in, and interaction with, the environment; whereas Γ_{nr} stands for any non-electromagnetic dissipation, i.e. an intrinsic relaxation. The presence of a layered structure affects the radiative decay Γ_{em} of the fluorophore because it modifies the local density of states (LDOS). For instance, a high index medium in the near field of the fluorophore increases the LDOS at the fluorophore position. In consequence, Γ_{em} increases, or equivalently the lifetime τ_{S_1} of the first excited singlet state S_1 is shortened, because more radiation modes are available. On the other hand, Γ_{nr} is assumed to depend only on the microenvironment of the fluorophore, e.g. it is not affected by the position and orientation dependent LDOS but rather by adsorption to a surface. In the following, the dissipated power P of a point dipole with fixed dipole moment $\vec{\mu}$ is calculated for two cases:

a) inside a homogeneous medium, e.g. far from interfaces, and

b) near a planar structured medium, e.g. near planar interfaces.

#94399 - $15.00 USD Received 28 Mar 2008; revised 9 May 2008; accepted 23 May 2008; published 27 May 2008

First, case (a) is calculated as reference for obtaining the radiative enhancement factor $\gamma(\vec{r},\Omega)$ in case (b). Because $\Gamma_{em} = P/\hbar\omega$, the radiative enhancement $\gamma(\vec{r},\Omega) = \Gamma_{em}(\vec{r},\Omega)/\Gamma_{em,\infty}$ is reproduced by the ratio $P(\vec{r},\Omega)/P_\infty$, where the subscript ∞ indicates the unperturbed case (a). In this context, we should keep in mind that the dissipated power describes the total power emitted via the dipole field, i.e. photon emission as well as radiative loss.

In the late seventies, Lukosz calculated the emission of electric and magnetic dipoles near a planar dielectric interface [19, 20]. In the eighties, Burghardt and Thompson [21] and Hellen and Axelrod [28] refined the calculation for TIRF microscopy. Recently, Novotny [23] revisited the theory for calculating the light field of interacting dipolar particles; and Mertz [24] unified the description of a classical dipole near a dielectric interface with a simple input–output formalism based on the Lorentz reciprocity theorem. The following description relies on the general ideas given by Ford and Webber [25]. This description is particularly advantageous because only the electric field at the dipole position is required for calculating the dissipated power, which circumvents any confusion in case of absorbing media (i.e. metals) in the vicinity of the dipole. According to Fig. 1, the total dissipated power of a point dipole at position $\vec{r}_0$ is given by

$$P = \frac{\omega}{2}\mathrm{Im}\left(\vec{\mu}^* \cdot \vec{E}(\vec{r}_0)\right) \tag{2}$$

where $\vec{\mu}$ is the dipole moment and $\vec{E}(\vec{r})$ the electric field radiated by this dipole. The dipole is described as a current source $\vec{j}(\vec{r}) = -i\omega\vec{\mu}\,\delta(\vec{r}-\vec{r}_0)$ in medium 1 and the radiated field has to fulfill the Maxwell equations.

$$\vec{\nabla}\times\vec{E}(\vec{r}) = \mu_0\frac{\partial}{\partial t}\vec{H}(\vec{r}) \qquad\qquad \vec{\nabla}\times\vec{H}(\vec{r}) + \epsilon_0\epsilon_1\frac{\partial}{\partial t}\vec{E}(\vec{r}) = \vec{j}(\vec{r}) \tag{3}$$

Using time harmonic fields and a plane wave expansion

$$\vec{E}(\vec{r}) = \int \vec{E}_k \exp(i\vec{k}\cdot\vec{r})\,\mathrm{d}\vec{k} \tag{4}$$

the Maxwell Eq. (3) read as

$$\vec{k}\times(\vec{k}\times\vec{E}_k) + k_1^2\vec{E}_k = -\omega^2\mu_0\vec{\mu}\,\delta(\vec{r}-\vec{r}_0)\,. \tag{5}$$

Solving for the electric field $\vec{E}_k$ propagating along the wavevector $\vec{k}$ yields

$$\vec{E}_k = -\mu_0\exp(-i\vec{k}\cdot\vec{r}_0)\frac{\omega^2}{k_1^2}\left(\vec{\mu} + \frac{\vec{k}\times(\vec{k}\times\vec{\mu})}{k^2-k_1^2}\right). \tag{6}$$

Substituting this expression in (4) and splitting the lateral and axial integration, an integral representation of the radiated field is obtained.

$$\vec{E}(\vec{r}) = -\mu_0\frac{\omega^2}{k_1^2}\int \mathrm{d}\vec{k}_{xy}\exp\left(i\vec{k}_{xy}\cdot(\vec{r}-\vec{r}_0)\right)\int_{-\infty}^{+\infty}\mathrm{d}k_z\left(\vec{\mu} + \frac{\vec{k}\times(\vec{k}\times\vec{\mu})}{k_z^2-k_{1z}^2}\right)\exp(ik_z(z-z_0)) \tag{7}$$

The k_z integral is a contour integral in the complex plane, which can be evaluated using the complex residues at the first order poles $k_z = \pm k_{1z}$. With $\vec{k}_1 = \vec{k}_{xy} + \vec{k}_{1z}(z-z_0)/|z-z_0|$, the electric field is then

$$\begin{aligned}\vec{E}(\vec{r}) = -2\pi\mu_0\frac{\omega^2}{k_1^2}\int \mathrm{d}\vec{k}_{xy}\exp\left(i\vec{k}_{xy}\cdot(\vec{r}-\vec{r}_0)\right)\\ \times\left\{\delta(z-z_0)\vec{\mu}_z + \frac{i}{2k_{1z}}\vec{k}_1\times(\vec{k}_1\times\vec{\mu})\exp(ik_{1z}|z-z_0|)\right\}\,.\end{aligned} \tag{8}$$

#94399 - $15.00 USD Received 28 Mar 2008; revised 9 May 2008; accepted 23 May 2008; published 27 May 2008

The first term does not contribute to the dissipated power because it is real valued. The second term is imaginary only for $k_{xy} < k_1$, which is the far field radiation domain in medium 1. Therefore, the dissipated power is obtained with (2) and

$$\vec{E}(\vec{r}_0) = -i\pi\mu_0 \frac{\omega^2}{k_1^2} \int\limits_{k_{xy}<k_1} \frac{\mathrm{d}\vec{k}_{xy}}{k_{1z}} \vec{k}_1 \times (\vec{k}_1 \times \vec{\mu}) \tag{9}$$

The electric field is now described by the coupling between the dipole moment $\vec{\mu}$ and the electric field $\vec{E}_k$, i.e. by a projection of $\vec{\mu}$ onto $\vec{E}_k$. Integrating over all directions of $\vec{k}_{xy}$ yields

$$P_\infty = \frac{\pi^2\mu_0\omega^3}{2k_1^2} \int_0^{k_1} \mathrm{d}k_{xy} \frac{k_{xy}}{k_{1z}} \left(2k_{xy}^2|\vec{\mu}_z|^2 + (2k_1^2 - k_{xy}^2)|\vec{\mu}_{xy}|^2\right), \tag{10}$$

and evaluates to the well-known Larmor formula, e.g. the dissipated power is given by

$$P_\infty = \frac{2}{3}\pi^2\mu_0\omega^3 k_1 |\vec{\mu}|^2 . \tag{11}$$

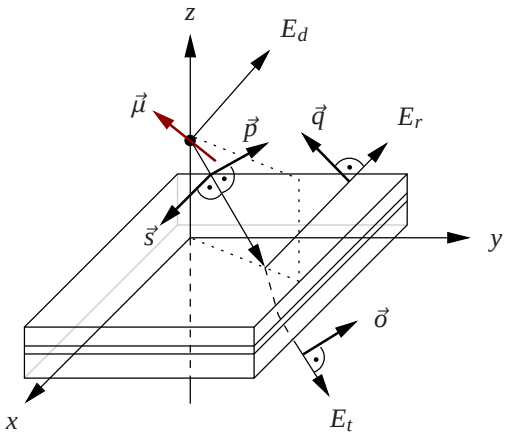

Fig. 2. Coupling of the dipole moment $\vec{\mu}$ with the electric fields. E_d represents the direct dipole field, E_r the reflected field and E_t the transmitted field. $\vec{s}$ is perpendicular to the incidence plane, whereas $\vec{p}$, $\vec{q}$ and $\vec{o}$ are parallel to the incidence plane.

In the second case (b) where the dipole is near to planar interfaces, the radiation towards the interfaces is partially reflected and interferes with the direct radiation $\vec{E}_d$ of the dipole as outlined in Fig. 2. The calculation involves the reflection coefficients $r_{1m}^{p,s}$ at the interfaces $n_1 \to n_m$ for *p*- and *s*-polarized fields $\vec{E}_k^{p,s}$. Therefore, the field in Eq. (8) is separated in the *p*- and *s*-polarized components using the vector identity

$$-\vec{k}_1 \times (\vec{k}_1 \times \vec{\mu}) = (\vec{p}\cdot\vec{\mu})\vec{p} + (\vec{s}\cdot\vec{\mu})\vec{s} \tag{12}$$

where $\vec{p} = k_{xy}\vec{e}_z + k_{1z}\vec{e}_{xy}$ and $\vec{s} = k_1\vec{e}_{xy} \times \vec{e}_z$ with the unit vectors $\vec{e}_{xy} = \vec{k}_{xy}/k_{xy}$ and $\vec{e}_z = (0,0,1)$. Hence, the first term gives the *p*-polarized component $\vec{E}_k^p$ and the second the *s*-polarized component $\vec{E}_k^s$. Using this in Eq. (8), the field propagating towards the interfaces is

$$\vec{E}^{\downarrow}(\vec{r}) = i\pi\mu_0 \frac{\omega^2}{k_1^2} \int \frac{\mathrm{d}\vec{k}_{xy}}{k_{1z}} \exp\left(i\vec{k}_{xy}\cdot(\vec{r}-\vec{r}_0) - ik_{1z}(z-z_0)\right)\{(\vec{p}\cdot\vec{\mu})\vec{p} + (\vec{s}\cdot\vec{\mu})\vec{s}\} . \tag{13}$$

#94399 - $15.00 USD Received 28 Mar 2008; revised 9 May 2008; accepted 23 May 2008; published 27 May 2008

The total field in the region $0 < z < z_0$ is this downward propagating dipole field plus an upward propagating reflected field. Upon reflection, the *p*-polarized component becomes proportional to $\vec{q} = k_{xy}\vec{e}_z - k_{1z}\vec{e}_{xy}$. Therefore, the total field in this region is

$$\vec{E}^{\downarrow\uparrow}(\vec{r}) = i\pi\mu_0 \frac{\omega^2}{k_1^2} \int \frac{\mathrm{d}\vec{k}_{xy}}{k_{1z}} \exp\left(i\vec{k}_{xy}\cdot(\vec{r}-\vec{r}_0) + ik_{1z}z_0\right)\times \\ \left\{(\vec{p}\cdot\vec{\mu})\left(\exp(-ik_{1z}z)\vec{p} + r_{1m}^p \exp(ik_{1z}z)\vec{q}\right) + (\vec{s}\cdot\vec{\mu})\left(\exp(-ik_{1z}z) + r_{1m}^s \exp(ik_{1z}z)\right)\vec{s}\right\} \tag{14}$$

where $r_{1m}^{p,s}$ are the reflection coefficients on the structure n_1 to n_m for *p*- and *s*-polarizations. The power dissipated by the dipole in the presence of the planar interfaces is obtained by inserting Eq. (14) in Eq. (2). Integrating over all directions of $\vec{k}_{xy}$, the dissipated power for a dipole at position $\vec{r}$ is

$$P(\vec{r},\Omega) = \frac{\pi^2\mu_0\omega^3}{2k_1^2}\,\mathrm{Re}\int_0^\infty \mathrm{d}k_{xy}\frac{k_{xy}}{k_{1z}}\left\{2k_{xy}^2\left(1 + r_{1m}^p\exp(2ik_{1z}z)\right)|\vec{\mu}_z|^2 \right. \\ \left. + \left[k_1^2\left(1 + r_{1m}^s\exp(2ik_{1z}z)\right) + |\vec{\mu}_{xy}|^2 k_{1z}^2\left(1 - r_{1m}^p\exp(2ik_{1z}z)\right)\right]|\vec{\mu}_{xy}|^2\right\} \tag{15}$$

The dissipated power in case (b) can be rewritten as P_∞ plus a contribution $\Delta P_z(\vec{r},\Omega)$ from $\vec{\mu}_z$ perpendicular to the structure and a contribution $\Delta P_{xy}(\vec{r},\Omega)$ from $\vec{\mu}_{xy}$ parallel to the interfaces. That is $P(\vec{r},\Omega) = P_\infty + \Delta P_z(\vec{r},\Omega) + \Delta P_{xy}(\vec{r},\Omega)$ with

$$\Delta P_z(\vec{r},\Omega) = \frac{\pi^2\mu_0\omega^3}{k_1^2}\,\mathrm{Re}\int_0^\infty \mathrm{d}k_{xy}\frac{k_{xy}}{k_{1z}}\exp(2ik_{1z}z)k_{xy}^2 r_{1m}^p|\vec{\mu}_z|^2 \quad \text{and} \tag{16}$$

$$\Delta P_{xy}(\vec{r},\Omega) = \frac{\pi^2\mu_0\omega^3}{2k_1^2}\,\mathrm{Re}\int_0^\infty \mathrm{d}k_{xy}\frac{k_{xy}}{k_{1z}}\exp(2ik_{1z}z)(k_1^2 r_{1m}^s - k_{1z}^2 r_{1m}^p)|\vec{\mu}_{xy}|^2\,. \tag{17}$$

Figure 3 shows results for a horizontal and a vertical dipole near an air–glass and a water–glass interface, respectively. The dissipated power is significantly enhanced if the dipole-interface

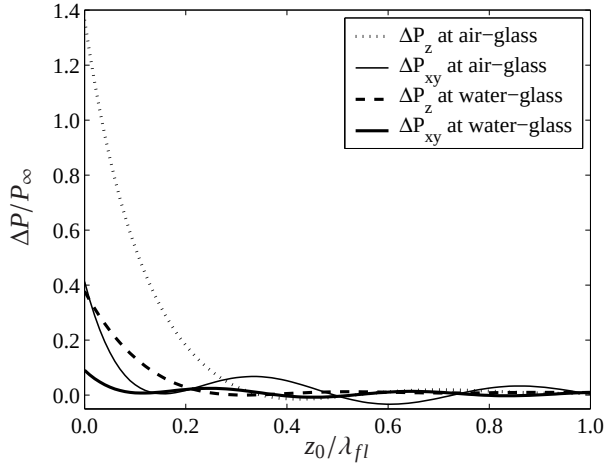

Fig. 3. Enhanced power dissipated by a vertical and a horizontal dipole near an interface.

#94399 - $15.00 USD Received 28 Mar 2008; revised 9 May 2008; accepted 23 May 2008; published 27 May 2008

distance is less than about $\lambda_{fl}/5$. For the horizontal dipole, the power enhancement shows an oscillation caused by the interferences between the direct and the reflected field in medium 1 (air, water). For the vertical dipole, the enhancement simply decreases with increasing distance (approximately exponentially). In addition, the enhancement is significantly stronger for the vertical dipole, which reflects the stronger coupling of the *p*-polarized near field in medium 1 to waves propagating at super-critical angles in the denser medium 2 (glass).

Now, the interaction of a fluorophore with planar interfaces can be calculated. Taking into account that $|\vec{\mu}_z| = |\vec{\mu}|\cos\Theta$ and $|\vec{\mu}_{xy}| = |\vec{\mu}|\sin\Theta$, the radiative enhancement factor $\gamma(\vec{r},\Omega)$ is given by $1 + \Delta P_z(\vec{r},\Omega)/P_\infty + \Delta P_{xy}(\vec{r},\Omega)/P_\infty$.

$$\gamma(\vec{r},\Omega) = 1 + \frac{3}{4k_1^3}\mathrm{Re}\int_0^\infty \mathrm{d}k_{xy}\frac{k_{xy}}{k_{1z}}\exp(2ik_{1z}z)\left\{2k_{xy}^2 r_{1m}^p\cos^2\Theta + (k_1^2 r_{1m}^s - k_{1z}^2 r_{1m}^p)\sin^2\Theta\right\} \quad (18)$$

In the limit $z \to \infty$, the integral vanishes which corresponds to the homogeneous case (a).

In general, the presence of the interface(s) in the vicinity of the fluorophore modifies its photophysical parameters and its emission pattern. For instance, the fluorescence quantum yield increases to

$$q'_{fl}(\vec{r},\Omega) = \frac{\gamma_{fl}(\vec{r},\Omega)\,q_{fl}}{\gamma_{fl}\,q_{fl} + 1 - q_{fl}} \quad (19)$$

where q_{fl} is the fluorescence quantum yield in case (a) and q'_{fl} in case (b). Because the radiative enhancement is anisotropic, the fluorophore emits more frequently when its dipole moment is oriented vertically to the glass–water/air interface. In summary, the vicinity of a planar structure affects the rate of the electromagnetic emissions of the fluorophore. This influence manifests itself as a modification of the excited state lifetimes as well as the transition probabilities. In the general case, the fluorescence emission rate R_{fl} is given by

$$R_{fl}(\vec{r},\Omega) = \frac{q'_{fl}}{\tau'_{S_1}}P'_{S_1} = \gamma_{fl}(\vec{r},\Omega)\frac{q_{fl}}{\tau_{S_1}}P'_{S_1}\,, \quad (20)$$

where τ_{S_1} is the lifetime of the excited singlet state S_1 and P'_{S_1} its occupation probability. But we should keep in mind that $R_{fl}(\vec{r},\Omega)$ is the radiation rate into different channels. This radiation is either transmitted to the far field in medium 1 or *m*, coupled to a wave-guide mode or surface plasmon, or absorbed in the structure. If the fluorophore approaches a metal for instance, its emission rate will significantly increase as well as q'_{fl} does. But this increased emission will be counter-balanced by an increased energy dissipation, i.e. due to electron-hole excitations in the metal. For a fluorophore–metal distance $\lesssim$ 20nm, the energy loss usually becomes so dominant that the observable fluorescence intensity is effectively lower than that far from the metal. These and many more effects are well described in literature (c.f. [26, 27, 28, 29] for example). Here, we concentrate on the calculation of the absolute detection efficiency. For that purpose, the emitted field is calculated next and then propagated to the pinhole.

3. Emitted dipole field

In this section, the far field emission is calculated in view of describing the collection efficiency by the microscope objective. For this purpose, the radiated far field is described as a plane wave spectrum according to Eq. (4). Analogous to Eq. (8), (13) and (14), it is given by the dipole field superimposed by the reflected field in medium 1, both propagating towards a collection

#94399 - $15.00 USD Received 28 Mar 2008; revised 9 May 2008; accepted 23 May 2008; published 27 May 2008

optics at $z > z_0$.

$$\vec{E}_k^{\uparrow\uparrow} = i\pi\mu_0 \frac{\omega^2}{k_1^2} \frac{\exp(-i\vec{k}_1 \cdot \vec{r}_0)}{k_{1z}} \times \left\{ \left(\vec{q} \cdot \vec{\mu} + (\vec{p} \cdot \vec{\mu}) r_{1m}^p \exp(2ik_{1z}z_0) \right) \vec{q} + (\vec{s} \cdot \vec{\mu}) \left(1 + r_{1m}^s \exp(2ik_{1z}z_0) \right) \vec{s} \right\} \tag{21}$$

The far field spectrum in medium m is given by the transmitted field propagating downwards. The Fresnel transmission coefficients through the structure are given by $t_{1m} = t_{m1} k_{1z}/k_{mz}$ and the field spectrum is

$$\vec{E}_k^{\downarrow\downarrow} = i\pi\mu_0 \frac{\omega^2}{k_1^2} \frac{\exp(-i\vec{k}_1 \cdot \vec{r}_0)}{k_{mz}} \left((\vec{p} \cdot \vec{\mu}) t_{m1}^p \vec{o} + (\vec{s} \cdot \vec{\mu}) t_{m1}^s \vec{s} \right) \exp(-ik_{mz}d) \tag{22}$$

where d is the total thickness of all layers and $\vec{o} = k_{xy}\vec{e}_z + k_{mz}\vec{e}_{xy}$.

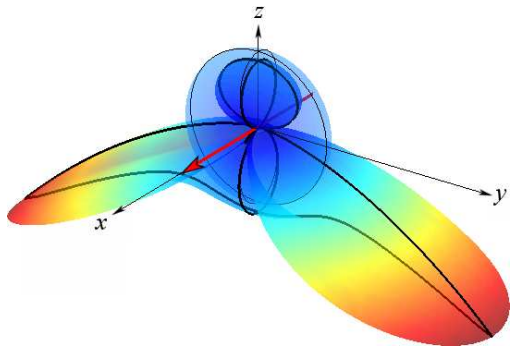

Fig. 4. Radiated angular power density $\propto |\vec{E}_k|^2$ for a horizontal dipole along the x-axis (arrow). The dipole is located at the glass–water interface.

Figure 4 shows the far field spectrum emitted by a horizontal dipole along the x-axis. In case (a), i.e. no interface, the dipole radiates homogeneously around its axis (thin lines outline the xz and yz cross-sections). In case (b), i.e. on a glass–water interface, the dipole radiates mainly into two lobes in the yz-plane (thick lines). The maximum radiation indicates the critical angle for total internal reflection at the interface. The total radiated power increases by less than 10%, but more than 69% of the radiation is directed into the glass. Compared with case (a), the radiated power is substantially increased in the glass whereas it is decreased by about 33% in the water.

The emitted field $\vec{E}_{fl}(\vec{r}, \Omega)$ is calculated from these far field spectra of a dipole at position $\vec{r}$ with orientation Ω. This representation as a $\vec{k}$ spectrum of the p- and s-polarized components is required anyhow for calculating the propagation to the detector in the next section. We would like to emphasize that it is important to consider the fluorophore as a *fixed power* dipole, whose power is imposed by the current emission rate. Therefore, we could require $P_{fl}(\vec{r}, \Omega) = R_{fl}(\vec{r}, \Omega)\hbar\omega_{fl}$ for normalizing the dipole moment $|\vec{\mu}(\vec{r}, \Omega)|$ right here. Instead, we include this normalization in the detection efficiency when dividing the detected power by $P_{fl}(\vec{r}, \Omega)$ for obtaining the detection efficiency $Q_{fl}(\vec{r}, \Omega)$.

4. Detection efficiency

The detection efficiency is considered as the complementary part of the excitation field. We define it by the probability of receiving a photon in the detection aperture (pinhole) if this photon was emitted at position $\vec{r}$ by a fluorophore with dipole orientation Ω. Figure 5 summarizes the

#94399 - $15.00 USD Received 28 Mar 2008; revised 9 May 2008; accepted 23 May 2008; published 27 May 2008

calculation of the detection efficiency $Q_{fl}(\vec{r},\Omega)$, which is accomplished by calculating the ratio $q_d T_{fl} P_p(\vec{r},\Omega)/P_{fl}(\vec{r},\Omega)$ with P_p the power transmitted through the pinhole. q_d is the quantum yield of the detector [30] and T_{fl} the transmission efficiency of the filter set [31], both at the fluorescence wavelength λ_{fl} (not shown).

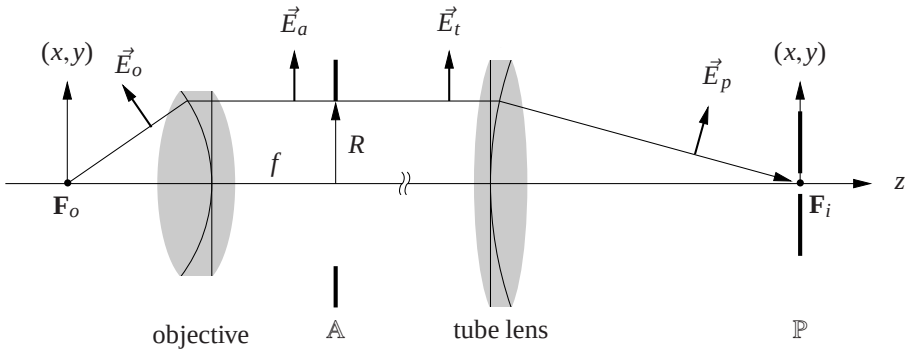

Fig. 5. Calculation of the electromagnetic field in the pinhole plane $\mathbb{P}$. The objective and the tube lens are represented by their principal planes (thin lines; refraction loci ≡ principal planes), the object focus $\mathbf{F}_o$, the aperture $\mathbb{A}$ in the back-focal plane of the objective, and the image focus $\mathbf{F}_i$.

$P_p(\vec{r},\Omega)$ is obtained by integrating the intensity falling on the pinhole. This requires calculating the electromagnetic field in the pinhole plane $\mathbb{P}$. Using the superscripts p and s for the p- and s-polarized components, the calculation of the field in the pinhole is subdivided into three distinct steps:

Step 1 The fluorescence emission is collected by the high NA objective.

The emitted field $\vec{E}_k$ in the direction of the wavevector $\vec{k}$ is calculated based on Eq. (21) or (22). The field $\vec{E}_o$ collected by the objective is essentially $\vec{E}_k$, but the phase is referenced to the object focus $\mathbf{F}_o$. Reversing the calculation of the excitation field in [14] leads to the field $\vec{E}_a$ in the objective aperture $\mathbb{A}$ (the reciprocity in optics was recently reviewed by Potton [32]). Considering medium n_m as the immersion medium allows us to identify $n_t = n_m$ and $k_t = k_m$. Recall that f and R are the focal length and the aperture radius of the objective with numerical aperture NA. Then, Eq. (1,8) in [14] read as

$$x,y = \frac{R}{k_0 \mathrm{NA}} k_{x,y} \qquad \text{and} \qquad \mathrm{d}\vec{k}_{xy} = \left(\frac{k_0 \mathrm{NA}}{R}\right)^2 \mathrm{d}x\,\mathrm{d}y\,. \tag{23}$$

The electric field arriving at the aperture $\mathbb{A}$ is therefore

$$E_a^{p,s}(x,y) = \frac{k_0 \mathrm{NA}}{R} t_{ta}^{p,s} E_o^{p,s}(k_x,k_y)\,. \tag{24}$$

The transmission coefficients t_{at} given by Eq. (21,22) in [14] were calculated from the aperture $\mathbb{A}$ to the immersion. For the reverse direction, they are given by $t_{ta} = n_t t_{at}$ ($\mathbb{A}$ is in air).

Figure 6(a) shows the electric field $|\vec{E}_a|$ in the aperture $\mathbb{A}$ of a 1.45 NA oil immersion objective observing a dipole in the focus at the cover slip–sample interface. For a x-oriented dipole (left), the field is relatively homogeneous at sub-critical angles (NA < 1.33). At super-critical angles, it exhibits a significant increase in particular perpendicular to the dipole axis, e.g. along the y-axis. Along the x-axis, the field vanishes right at the critical angle. The vertical dipole (right) emits a rotationally symmetric field (p-polarized), which is particularly strong at super-critical angles.

#94399 - $15.00 USD Received 28 Mar 2008; revised 9 May 2008; accepted 23 May 2008; published 27 May 2008

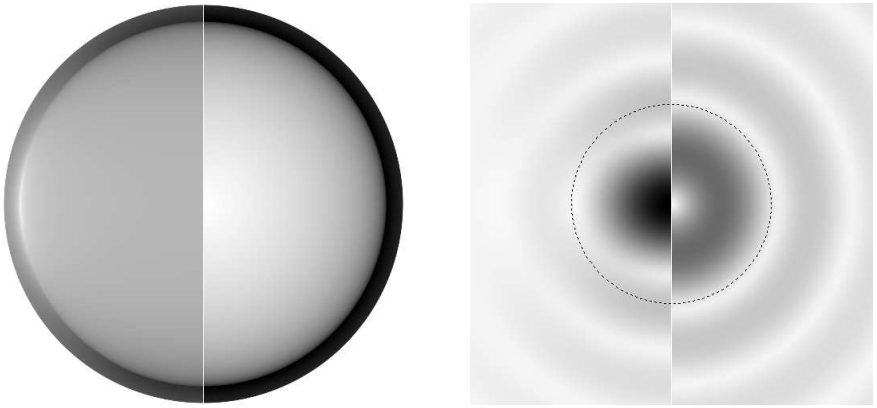

(a) Electric field $|\vec{E}_a|$ in the aperture $\mathbb{A}$.

(b) Electric field $|\vec{E}_p|$ at the pinhole $\mathbb{P}$.

Fig. 6. Electric fields in the aperture of a 100×1.45 NA oil immersion objective (a) and at the pinhole (b) for a dipole at the cover glass–sample (water) interface emitting at a wavelength of $\lambda_{fl} = 525$nm. The circle in (b) indicates a pinhole of 50µm in diameter. The left half-pictures show the field of the horizontal dipole. The field of the vertical dipole is shown in the right half-pictures.

Step 2 The fluorescence emission is propagated to the tube lens.

Because the field distribution in $\mathbb{A}$ can be described as paraxial and the propagation distance $z_p - z_a \gtrsim 120$mm, the Fresnel approximation for this free space propagation can be applied. In general, the Fresnel approximation is valid for

$$(z_p - z_a)^3 \gg \frac{\pi}{4\lambda} \max\left((x_a - x_p)^2 + (y_a - y_p)^2\right)^2 . \tag{25}$$

This is a sufficient condition, which would demand a propagation distance $z_p - z_a \gtrsim 500$mm. However, if the main contribution of the field $\vec{E}_t$ at point (x_p, y_p, z_p) comes from points (x_a, y_a, z_a) close to (x_a, y_a, z_p), i.e. for paraxial fields, the Fresnel approximation is also valid for smaller propagation distances. This is achieved with the pseudo-paraxial Fresnel transformation for removing the wave front tilt [33] and an equivalent transform [34, 35] for reducing the wave front curvature.

In a first order approximation, this entire step can be skipped by setting the field $\vec{E}_t$ on the tube lens equal to the field $\vec{E}_a$ at the objective.

Step 3 The fluorescence emission is focused onto the pinhole.

The field $\vec{E}_p$ near the image focus $\mathbf{F}_i$ in the pinhole plane is calculated with the Debye diffraction integral following the method by Leutenegger et al. [14]. If the focusing angles are small, the Fraunhofer approximation may be used.

Figure 6(b) shows the electric field $|\vec{E}_p|$ at the pinhole $\mathbb{P}$. The image of the horizontal dipole resembles a deformed Airy pattern, whereas the field of the vertical dipole is strongest in a ring around the axis (donut with small z-polarized component in the center).

Integration of the intensity $I_p = \sqrt{\epsilon_0/\mu_0}|\vec{E}_p|^2/2$ over the clear aperture of the pinhole and normalization by the emitted power $P_{fl}(\vec{r},\Omega)$ yields finally the detection efficiency $Q_{fl}(\vec{r},\Omega)$ for an arbitrary position $\vec{r}$ and orientation Ω of the fluorophore. If we assume random orientation with

#94399 - $15.00 USD Received 28 Mar 2008; revised 9 May 2008; accepted 23 May 2008; published 27 May 2008

a uniform probability $P(\Omega) = 1/4\pi$, the average detection efficiency is calculated as

$$Q_{fl}(\vec{r}) = \int_{\Omega} Q_{fl}(\vec{r},\Omega)P(\Omega)\,\mathrm{d}\Omega \approx \frac{1}{3}\left(Q_{fl}(\vec{r},\Omega_x) + Q_{fl}(\vec{r},\Omega_y) + Q_{fl}(\vec{r},\Omega_z)\right) . \qquad (26)$$

In general, the energy flux through the aperture is given by integrating the normal component of the Poynting vector $\langle\vec{S}\rangle = \langle\vec{E}\times\vec{H}\rangle$ over the aperture area (see e.g. Eq. (21) by Enderlein et al. [6]). As we consider standard microscopes, the image NA is in general less than 0.05 [36], which yields a relative error $1 - \cos\mathrm{NA} < 0.2\%$ if I_p is taken instead of $\langle\vec{S}\rangle$.

5. Results

Figure 7(a) shows the average detection efficiency for a 100×1.45 NA oil immersion objective observing randomly oriented fluorophores emitting at a wavelength $\lambda_{fl} = 525$nm near the glass–sample interface. The projected pinhole diameter is 0.5μm on the interface, which results

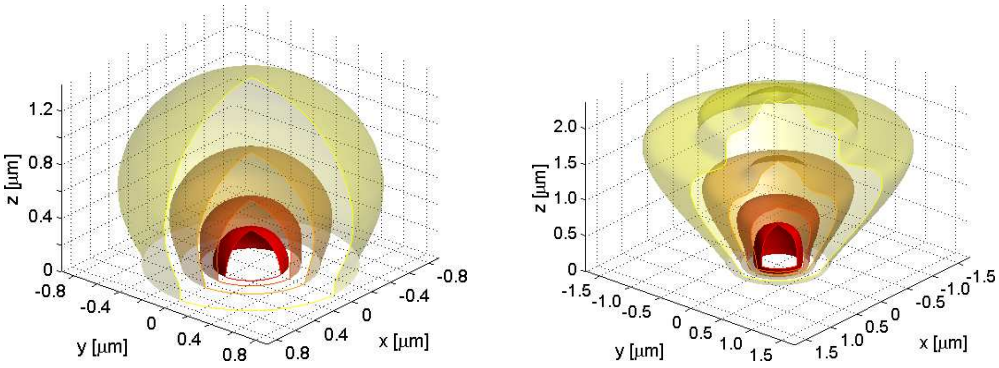

(a) Detection efficiency of a 100×1.45 NA oil immersion objective focused on the cover glass–water interface. The detection pinhole has a diameter of 50μm.

(b) Detection efficiency of a 40×1.20 NA water immersion objective focused on the cover glass–water interface. The detection pinhole has a diameter of 25μm.

Fig. 7. Detection efficiency (through the cover glass) of isotropically oriented fluorophores achieved with two immersion objectives focused on the cover glass–water interface. The iso-surfaces show the efficiencies $Q_{fl}(\vec{r}) = e^{-1\ldots-4}Q_{fl}(0)$ in the sample. The oil immersion objective (a) has a peak detection efficiency of ≈ 24% and the water immersion objective (b) of ≈ 14%.

in a hemi ellipsoidal detection volume of 0.7μm base diameter and 0.5μm axial extension. Assuming $q_d T_{fl} = 1$ [37], the peak detection efficiency at the interface is about 24%, which is 2–3× better than with the following 1.20 NA water immersion objective.

The detection efficiency of a 40×1.20 NA water immersion objective at identical conditions is shown in Fig. 7(b). The projected pinhole diameter is 0.6μm on the interface and the peak efficiency is about 14% (65nm in the sample, ≈ 13% at the interface). The detection volume has a base diameter of 0.8μm and an axial extension of 0.8μm into the sample. No super-critical light is collected and the water immersion matches the refraction index of the sample, which results in a detection volume extending significantly deeper into the sample than with the oil immersion objective.

Figure 8(a) compares the detection efficiency for the outlined cases whereas Fig. 8(b) compares the performance of the water immersion objective for epi- and trans-illumination, that is for collection from the glass side and, respectively, the sample side. The detection efficiency with trans-illumination shows the typical undulations due to interferences between the direct

#94399 - $15.00 USD Received 28 Mar 2008; revised 9 May 2008; accepted 23 May 2008; published 27 May 2008

and the reflected radiation. The 1.20 NA objective collects up to about 15% at a distance of 120nm from the interface, whereas it collects $\lesssim 12\%$ on the interface. Such a trans-illumination configuration is often used in combination with TIRF (c.f. also Lieto et al. [38]), but is of advantage only if the observed fluorophores are at a distance of about $\lambda_{fl}/5$ from the glass interface.

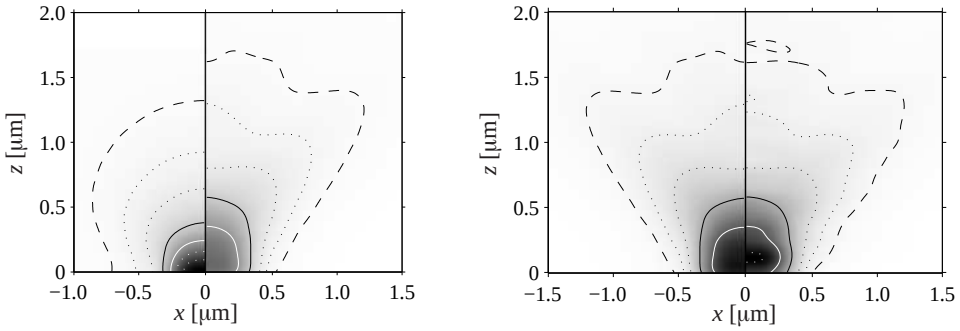

(a) 100×1.45 NA oil immersion (left) and $40\times$ 1.20 NA water immersion objective (right).

(b) 40×1.20 NA water immersion objective on the glass side (left) and the sample side (right).

Fig. 8. Detection efficiency of isotropically oriented fluorophores for immersion objectives focused on the cover glass–sample interface. White dotted lines outline an efficiency of 20% and 15%, white solid lines of 10%, black solid lines of 5%, dotted lines of 2% and 1% and ticked lines of 0.5%, respectively.

6. Conclusions

We presented a complete framework for accurately calculating the detection efficiency of fluorescence emission at interfaces. Our calculation accounts for the spatial distribution of the emitted fluorescence and yields the absolute detection efficiency defined as the probability of collecting an emitted photon. We presented examples for fluorescence detection at a glass–water interface and compared the detection yields for total internal reflection fluorescence microscopy in epi- and trans-illumination. These calculations clearly show the superiority of the 1.45 NA objective for epi-TIRF, firstly because it outperforms the detection efficiency as well as the resolution of the 1.20 NA objective and, secondly, because it is able to provide an evanescent illumination without further equipment. We recently introduced epi-TIRF for fluorescence correlation spectroscopy (FCS) and showed experimentally a 2–3× increase of the molecular brightness [39, 40], which we attributed to the high detection efficiency in combination with an increased emission rate and an enhanced intensity in the evanescent excitation field. Our experimental findings fully support the presented calculations. Together, the focus field and detection efficiency calculations foster the understanding of existing concepts in fluorescence microscopy, but proved to be an indispensable element for quantitative microscopic molecular investigations.

Acknowledgments

This work is part of the FuSyMEM project funded by the European Commission.

#94399 - $15.00 USD Received 28 Mar 2008; revised 9 May 2008; accepted 23 May 2008; published 27 May 2008